Study of polycyclic aromatic hydrocarbons (PAHs) in hydrogen-enriched methane diffusion flames

Chinonso Ezenwajiaku[1], Midhat Talibi[1*], Nguyen Anh Khoa Doan[2], Nedunchezhian Swaminathan[2], Ramanarayanan Balachandran[1*]

[1] *Department of Mechanical Engineering, University College London, Torrington Place, London WC1E 7JE, United Kingdom*

[2] *Department of Engineering, University of Cambridge, Trumpington Street, Cambridge CB2 1PZ, United Kingdom*

Abstract

Polycyclic aromatic hydrocarbons (PAHs) are the carcinogenic components of soot. Detailed understanding of PAH formation characteristics is required for development of effective strategies to curtail PAH formation and reduce soot in combustion devices. This study presents an experimental methodology to analyse PAH formation characteristics of a non-premixed methane-air flame with and without hydrogen (H_2) addition, using simultaneous planar laser induced fluorescence (PLIF) imaging of PAH and hydroxyl radical (OH). OH PLIF was used to represent peak temperature regions in the flame front. One-dimensional, opposed-jet laminar non-premixed flame simulations were also carried out for the same fuel mixture conditions. This work describes comparison of trends from both sets of studies. PAH fluorescence intensity values were observed to increase with increasing height above burner, however this rate of increase reduced with H_2 addition. This observed rate of change in PAH fluorescence (that is, PAH growth characteristics) is indicative of the sooting potential of the fuel mixture. PAH fluorescence from experiments and PAH concentration from simulation show strong reduction with increase in H_2 addition. The percentage reduction in PAH fluorescence signal with H_2 addition closer to the burner tip was of a similar magnitude to that observed with flame simulations. The reduction in PAH with H_2 addition could be attributed to the reduction in acetylene and propargyl concentrations, and reduced H-abstraction rates, which reduced the availability of active sites for PAH growth. The proposed experimental methodology for PAH measurements can be readily applied to any fuel mixtures.

Keywords: Polycyclic aromatic hydrocarbons; soot; hydrogen; inverse diffusion flames; PLIF; OH

* Corresponding authors. Email address: m.talibi@ucl.ac.uk, r.balachandran@ucl.ac.uk

1. Introduction

Anthropogenic activities are a major source of air pollution globally due to exhaust emissions from automobiles, aircrafts and industrial plants. Soot has been identified as a particularly toxic emission due to the presence of polycyclic aromatic hydrocarbons (PAHs) that are adsorbed on exhaust soot particles. PAHs are precursors of soot and consist of two or more benzene rings arranged in a variety of configurations. PAHs can persist long-term in the environment, often being carried over long distances without degradation. As an example, PAHs emitted in the UK have been detected as far as southern Norway [1]. Chronic exposure to PAHs is toxic to humans due to their carcinogenic properties by which PAHs induce mutagenic changes in human DNA, resulting in various malignancies, along with other adverse health effects such as weakened immune system and impaired lung function [2,3]. Hence, PAHs have been identified as serious health hazards, with various agencies, such as USEPA (United States Environmental Protection Agency) and IARC (International Agency for Research on Cancer), classifying PAHs with 2-6 rings having the most toxic potential.

In order to develop effective measures to reduce the toxicity of exhaust, it is essential to understand the complex processes which lead to PAH formation, and subsequent soot production. Open flame configurations can provide vital information in this regard, and both premixed and non-premixed flames have been used [4–11]. However, non-premixed flames have been observed to be more suitable to effectively track the early stages of PAH formation (such as acetylene production), and to understand the effect of fuel molecular structure on soot production [12]. In addition, it has also been observed that it is possible to classify PAHs based on their sizes in diffusion flames, which is not feasible in premixed flames [13]. Two types of non-premixed flame configurations are commonly used for PAH studies, normal diffusion flames (NDF) and inverse diffusion flames (IDF); in the NDF configuration the central fuel flow is surrounded by the oxidiser, while the configuration is reversed in IDF. Blevins et al.[14] established the similarity in the chemical and morphological properties of soot formed from both flames. However, investigations have reported difficulties in studying particle precursor formation in NDF because the combustion products convect towards the main reaction zone of the flame and get oxidised [4,5]. On the other hand, the IDF configuration favours the formation of relatively larger amounts of PAHs and soot, as the combustion products get formed on the fuel-rich side of the flame and avoid undergoing significant oxidation. Furthermore, a study by Dobbins [15] observed that nanoparticles sampled from inverse diffusion flames (IDF) had similar chemical composition to those found in diesel engine exhaust. Hence, the IDF configuration is more suitable for the study of PAHs, and relevant to real world combustion applications.

A variety of optical and non-optical techniques exist to study PAHs produced during combustion, and to provide information regarding their speciation and concentrations. The use of the non-intrusive planar laser induced fluorescence (PLIF) technique to detect PAHs in open flames is preferred over intrusive

techniques (such as collecting samples using microprobes or microfilters), as it does not interfere with the flow field or disrupt concentration profiles [16], and can provide qualitative spatially and temporally resolved details of PAH formation in the flame. Several studies have successfully employed the laser induced fluorescence (LIF) technique in the study of PAH formation [6–8,17]. Liu et al. [9] studied the effect of doping laminar gasoline flames (in a NDF configuration) with various alcohols (methanol, ethanol and n-butanol) on PAHs using PLIF. They observed that increasing the alcohol ratio decreased PAHs monotonously with methanol reported as having most significant effect in inhibiting the PAH growth process. Yamamoto et al. [18] compared the PAH LIF signal with quantitative PAH concentrations obtained using the Gas Chromatography/Mass Spectrometry (GC/MS) sampling technique in a propane flame in IDF configuration. The authors reported a good correlation between the profiles of the PAH LIF signal and the quantitative concentrations of benzene and naphthalene.

Many researchers have investigated experimentally the addition of secondary gases (hydrocarbon and non-hydrocarbon) to hydrocarbon flames to reduce PAH formation [10,11,19–23] and soot [24–31]. Zhang et al. [10] investigated the effect of adding CO_2 and water vapour in ethylene/oxygen/argon flames on PAH formation, and reported a monotonic decrease in PAH LIF signal intensities as the proportion of CO_2 and water vapour (H_2O) were increased. In addition, the authors observed greater PAH reductions with water vapour addition as compared to CO_2. The authors suggested the following explanation for this observation. The addition of CO_2 reduced the reaction rate of the $CO + OH \leftrightarrow CO_2 + H$, depleting the concentration of the H radical and increasing OH concentration, thereby enhancing oxidation rates. However, the addition of water vapour reduced the forward reaction rate of $OH + OH \leftrightarrow O + H_2O$ and $CH_3 + OH \leftrightarrow CH_2^* + H_2O$, resulting not only in increased OH concentrations, but also reduced benzene concentrations (and hence supressed PAH formation). Wu et al. [11] studied the addition of dimethyl ether (DME) to ethylene-air premixed flames, and concluded that the reduction in PAHs could be attributed to both the increase in the concentrations of oxidising radicals, OH and O, and the decrease in the amount of carbon that is available to form PAHs. The experimental results were in good agreement with modelling work done in the same study. Park et al. [28] showed that the addition of toluene to n-heptane resulted in a linear increase in PAH LIF signal, attributable to the increase in benzyl radicals as the proportion of toluene was increased in the mixture. Hydrogen (H_2) addition has been found to reduce particulates significantly both in open flame configurations [24,25,27] and combustion engines [32–34]. Previous studies exist which have used computational models to understand PAH growth mechanisms in hydrocarbon flames with H_2 addition [26,35] . Guo et al. [26] observed that H_2 addition resulted in a reduction in PAHs through both dilution and chemical inhibition effects. The added H_2 reduced the concentration of atomic H in the surface growth region and increased the amount of molecular H_2 in the close to the burner surface. This resulted in lower H-abstraction rates in the PAH and soot surface growth processes. This observation was supported by another numerical study conducted by Park et al. [35] which reported that, close to the burner surface,

the rate of forward reaction of $OH + H_2 \leftrightarrow H_2O + H$ increased with increasing H_2 addition, thereby increasing the concentration of the H radical in the reaction zone (and reducing PAH growth). Moreover, it was also observed that the concentration of acetylene was lower close to the burner surface which impeded benzene (and subsequently PAH) formation. The concentration of benzene increased with increasing height above the burner, but the rate of formation of larger PAHs was reported to reduce, attributed to the addition of H_2 which decreased H-abstraction rates, and hence reduced the number of sites available for acetylene addition. As outlined in the studies above, hydrogen H_2 chemically interferes with PAH formation reactions, and therefore could be a viable candidate for reducing both PAH and soot emissions.

The review of literature shows that while there are a number of computational studies which show a positive effect of adding H_2 on soot and PAH reduction, there is a lack of systematic experimental work to understand the effects of H_2 addition on PAH formation. The current work will focus on developing a methodology to study PAH growth characteristics and, for the first time in the authors' view, present a comparison between experimental and computational studies in methane-hydrogen diffusion flames. The objectives of the current study are: (1) to systematically investigate PAH formation characteristics of non-premixed methane-air flames, (2) to understand the effect of H_2 addition on PAH formation in the methane-air flames and (3) to compare the experimental results with 1-D flame simulations utilising detailed chemical mechanisms. The paper first describes the experimental hardware and methodology utilised in this work, before explaining the image processing procedures employed in this work. Details regarding repeatability and comments related to uncertainties in the methodology are then provided. Detailed discussions of experimental and computational results for methane-air and methane-hydrogen-air flames are presented before providing a summary of key conclusions.

## 2. Methodology

2.1. Burner
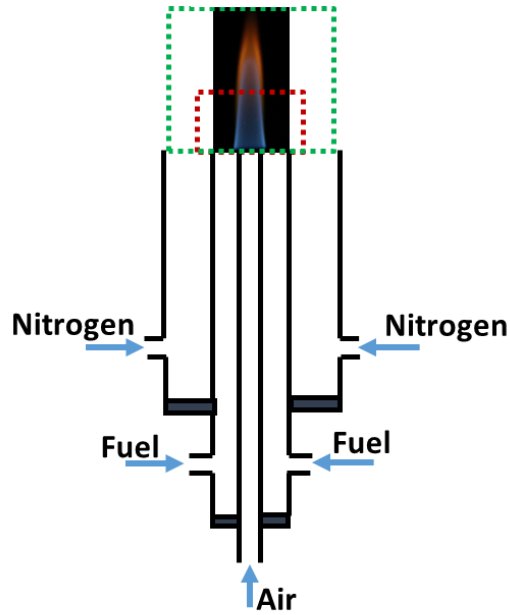
Fuel = Primary (CH$_4$) + Secondary (H$_2$)

Figure 1: Schematic of the burner showing a typical flame and imaging area for PAH 'zoomed in' (red dotted lines, FOV - 34 mm x 26 mm) and 'zoomed out' (green dotted lines, FOV - 76 mm x 56 mm) configurations.

The burner used for this study is based on inverse diffusion flame (IDF) configurations utilised in literature [7,14], and a schematic of the burner is shown in Figure 1. The burner consists of three coaxial stainless steel tubes, with the inner and outer co-flow forming consecutive annular passages around the central tube. The inside diameters of the central, inner co-flow and outer co-flow passages were 10, 30 and 64 mm respectively. To reduce the effect of rim thickness, the burner exit was tapered to a knife edge for all the three tubes. A combination of steel balls (of diameters 3 mm and 5 mm), wire mesh and honeycomb were utilised for flow smoothening and straightening for the co-flow gases.

The air and fuel passed through central and inner co-flow passages respectively, allowing stabilisation of an inverse diffusion flame, IDF. The flame was shrouded from ambient air by nitrogen, flowing in the outer co-flow passage, to minimise air entrainment effects. The effect of hydrogen (H$_2$) addition was studied by premixing desired quantities of H$_2$ considerably far upstream (approximately 1400 mm) of the burner exit. Thermal mass flow meters (Vögtlin Instruments) fitted with high precision needle valves were used for independent control and metering of all gas flows (air, methane, hydrogen and nitrogen) to the burner. The accuracy of all the flow meters was ±1.5% full scale division (FSD).

2.2.   Simultaneous OH and PAH LIF imaging
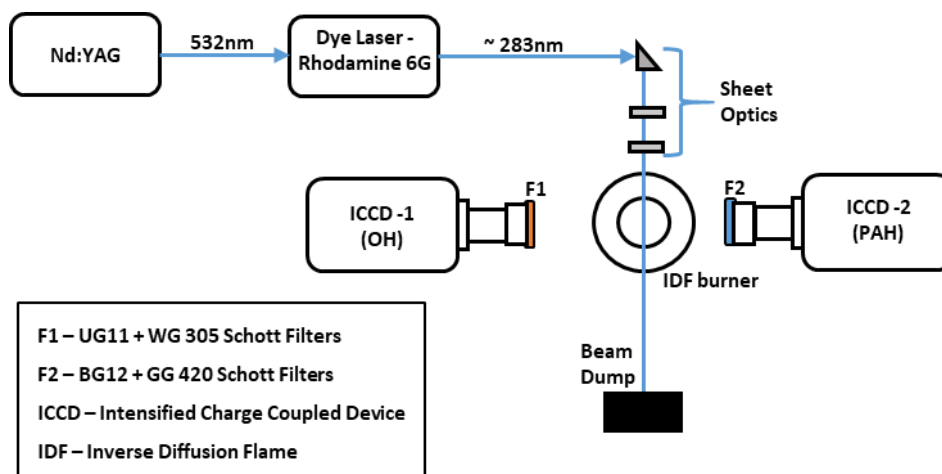
Figure 2: Schematic of the experimental arrangement used for simultaneous planar laser induced fluorescence imaging of PAH and OH.

The schematic for the laser and camera setup is shown in Figure 2. For the excitation of the OH radical, a frequency-doubled output from an Nd:YAG Laser (Litron Nano-PIV) was used to pump a tunable dye laser (Fine Adjustments Pulsare-S model) with Rhodamine 6G dye. The output from the dye laser was frequency-doubled and tuned to near 283 nm to obtain the Q1(5) transition of the $A^2\Sigma^+ \leftarrow X^2\prod$ (1,0) band with approximately 12 mJ pulse energy. A combination of a right-angle prism, plano-concave cylindrical lens (f= -40 mm) and bi-convex lens (f= 500 mm) was used to convert the beam to a light sheet with height of 50 mm and thickness of 0.15 mm determined by the scanning knife edge technique [5]. The location of the sheet was adjusted to coincide with the central axis of the burner.

The same laser sheet was also used for excitation of the PAH species. It was noted from literature that PAH LIF emissions are insensitive to excitation wavelength in the range between 265 and 297 nm [36]. The interference from soot particles, due to resonant radiation from laser induced incandescence, on PAH LIF measurement in diffusion flames is well-known [21,29,37,38]. A simple soot isolation technique, described in [39], was used to measure the amount of soot present in the flames; no interference from soot was observed at the flow conditions used in this study in the region of interest (ROI).

The fluorescence from the OH radicals and PAH species were imaged simultaneously by two intensified charge coupled devices (ICCDs) placed perpendicular to the direction of the laser sheet on either side of the burner (Figure 2). The OH fluoresced near 310 nm and was captured on ICCD-1 (see Figure 2) which was fitted with a UV 100 mm f/2.8 Cerco lens and a combination of UG11 and WG305 Schott glass filters.

For the PAH species, the fluorescence was captured on ICCD-2 (Figure 2) using lens of two different focal lengths. A f/2.8 Nikon lens of focal length 105 mm was used to image a larger part of the flame (FOV- 76 mm x 56 mm) with a pixel projection resolution of 25 μm. While, a f/1.2 Nikon lens of focal length 50 mm was used to image up to 26 mm of the flame height hence providing a higher resolution image of the lower part of the flame closer to the burner lip (FOV- 34 mm x 26 mm, pixel projection resolution- 56 μm). The two focal length arrangements will from here on be referred as the 'zoomed out' and 'zoomed in' configurations, and have been illustrated in Figure 1 using green and red dotted lines, respectively. A combination of GG420 (high pass Schott filter) and BG12 (low pass Schott filter) fitted to the lens to image fluorescence from PAH species of three or more rings between the wavelength range of 420 nm and 480 nm.

The emitted PAH LIF spectra are heavily influenced by variations in temperature and the concentration of species in the surrounding atmosphere [40]. Hence, it is not yet possible to determine the concentrations of individual PAH species based on the emitted fluorescence signal [41]. Rather, the obtained LIF signal collectively represents a mixture of PAH species, often differentiated for specific sizes based on the collection wavelength range. Most PAH species absorb strongly over a wide range of excitation wavelengths from UV to visible [13,42] with the corresponding emission wavelength dependent on the number of aromatic rings possessed by the PAH molecule, and increasing with the number of aromatic rings [11,21,43]. Vander Wal *et al.* [44] reported that with excitation wavelength below 300 nm, PAH with 2 or 3 aromatic rings can fluoresce between 300-350 nm while PAHs of 4 rings or more can exhibit fluorescence in the range 300-700 nm. More specifically, investigations in [11,43] assigned PAH fluorescence in the visible range of 400 – 480 nm to larger PAHs of 3 to 5 rings.

The temperature dependence of a given PAH LIF signal primarily arises from the collisional quenching and the Boltzmann population fraction [45]. Since the LIF signal being obtained in this work represents a mixture of PAHs of three to five rings, the absorption and emission spectral characteristics of the PAHs can be assumed to be largely similar. There is no data available in literature outlining the variation in the quenching characteristics of PAH species with temperature in the range of interest [37,46]. However, flame simulation analysis performed for this work shows that the peak PAH occurs at a narrow temperature range $(1540 \pm 20K)$ for all the H_2 addition levels considered in this study – the data has been presented in Table 1. It was also observed from the flame simulation studies that the range of temperature remained similar for the different H_2 addition cases, and therefore it can be assumed that the Boltzmann constant would remain constant for the different test cases. In this study, it has been assumed that the quenching characteristics would remain constant for all the experiments conducted in this study. Hence, it can be concluded that the PAH LIF signal would be primarily dependent on the number density of the PAH species present in the flame. Furthermore, the PAH LIF technique will be suitable for this work as it focusses on the relative comparison in PAH formation characteristics with different levels of H_2 addition.

2.3. 1-D Flame calculations

To model the flame structure in regions away from the heat loss region and the top curved region of a laminar inverse diffusion flame, counter-flow laminar flames calculations at a pressure of 1 atm have been performed using CANTERA [47]. The chemical reactions are modelled using the Appel-Bockhorn-Frenklach gas-phase mechanism [48]. This mechanism was used as it includes some aromatic species and has been well validated for C_1-C_2/air combustion. The fuel stream for the counter-flow was composed of CH_4 or CH_4 enriched with H_2 depending on the case under study, while the oxidiser stream was air. Both streams were set at a temperature of 298 K, and, for all cases, the strain rate was set to a small value (below 10 s^{-1}) to ensure a fully reacting solution which is of interest here. These computational calculations obtained allowed for qualitative comparison with the experimental results.

2.4. Flow conditions

H_2 addition (lpm)	% H_2 addition	T at [PAH]$_{max}$ (K)	T_{max} (K)	w_{OH} experiments (mm)	$w_{[OH]}$ simulations (mm)
0	0	1520	2152	2.61	3.41
0.2	2	1530	2159	2.51	3.41
0.4	4	1540	2165	2.50	3.27
0.6	6	1550	2171	2.51	3.41
0.8	8	1520	2178	2.44	3.41
1	10	1540	2184	2.56	3.55
1.2	12	1550	2190	2.91	3.62
1.4	14	1560	2196	2.83	3.41
1.6	16	1530	2202	2.69	3.48
1.8	18	1540	2208	2.98	3.62
2	20	1550	2213	2.81	3.69

Table 1: Hydrogen flow rates (Q_{H_2}) at corresponding percentage H_2 addition (Q_{H_2}/Q_{CH_4}) for fixed Q_{CH_4} (10 lpm) and Q_{air} (1.5 lpm) flow rates. The temperature at maximum PAH concentration (*T* at [PAH]$_{max}$) and the maximum flame temperature (*T$_{max}$*) is also shown for each H$_2$ addition.

For all the tests conducted in this study, the flow rate of methane (CH_4), Q_{CH4}, and of air, Q_{air}, were fixed at 10 lpm and 1.5 lpm, respectively. Hydrogen (H_2) was added to the CH_4 flow line, well in advance of the flame location to ensure proper mixing. The flow rate of hydrogen (Q_{H2}) was changed with the resolution of 0.2 lpm. Up to 2 lpm of H_2 was added to the CH_4, which is 20% by volume of CH_4. The same mole fraction of fuel mixture (methane and hydrogen) served as input to 1D flame calculations. In addition, Table 1 also shows the temperature at maximum PAH and the maximum temperature, both obtained from the flame simulation work. These temperatures will be referred to in later sections of the paper.

3. Image processing
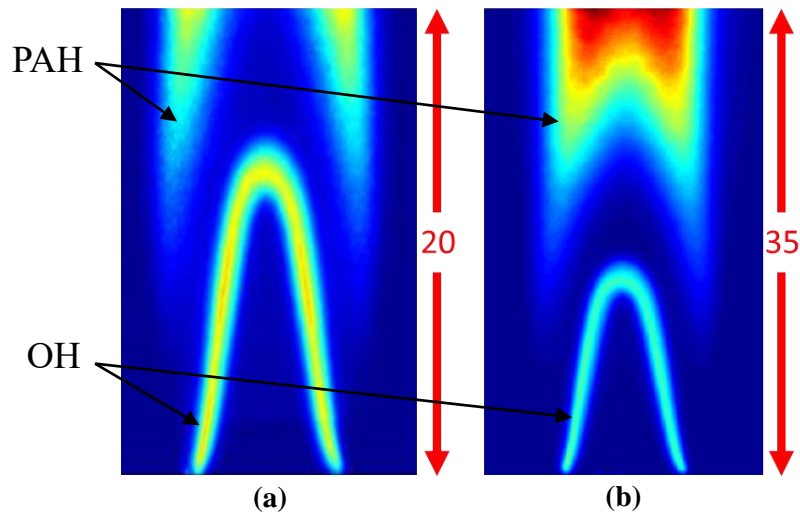
Figure 3: Illustrations showing resolution-adjusted, averaged and combined PLIF images of OH and PAH for the (a) zoomed in and (b) zoomed out configurations (only the region of interest, ROI, is shown).

Figure 3 shows the averaged combined images of PAH and OH for the two different focal length imaging arrangements, zoomed in and zoomed out (as described in Section 2.2). It should be noted that the captured LIF images have been cropped to only show the region of interest (ROI) in Figure 3. The PAH and OH LIF images were captured by two separate ICCD cameras (see Figure 2), with 400 instantaneous images captured for each test condition. A software median filter was used on the instantaneous images to reduce noise. The filtered instantaneous images were then background corrected and averaged to obtain averaged PAH and averaged OH images for each test condition. As the pixel projection resolution of OH and PAH images are different, the OH image was then transposed (with sub-pixel accuracy) onto the PAH image using an in-house developed image warping MATLAB® code. The resolution-adjusted images of OH and PAH had common coordinates and were kept separately for further processing to obtain information regarding PAH formation characteristics. The combined images are presented in Figure 3 (the purpose of the illustration is to show spatial alignment, hence the colour scales are arbitrary). Two different image processing approaches were employed to obtain PAH formation characteristics, as described in the following sections.

3.1.   Change in PAH with respect to flame position (flame normal statistics)
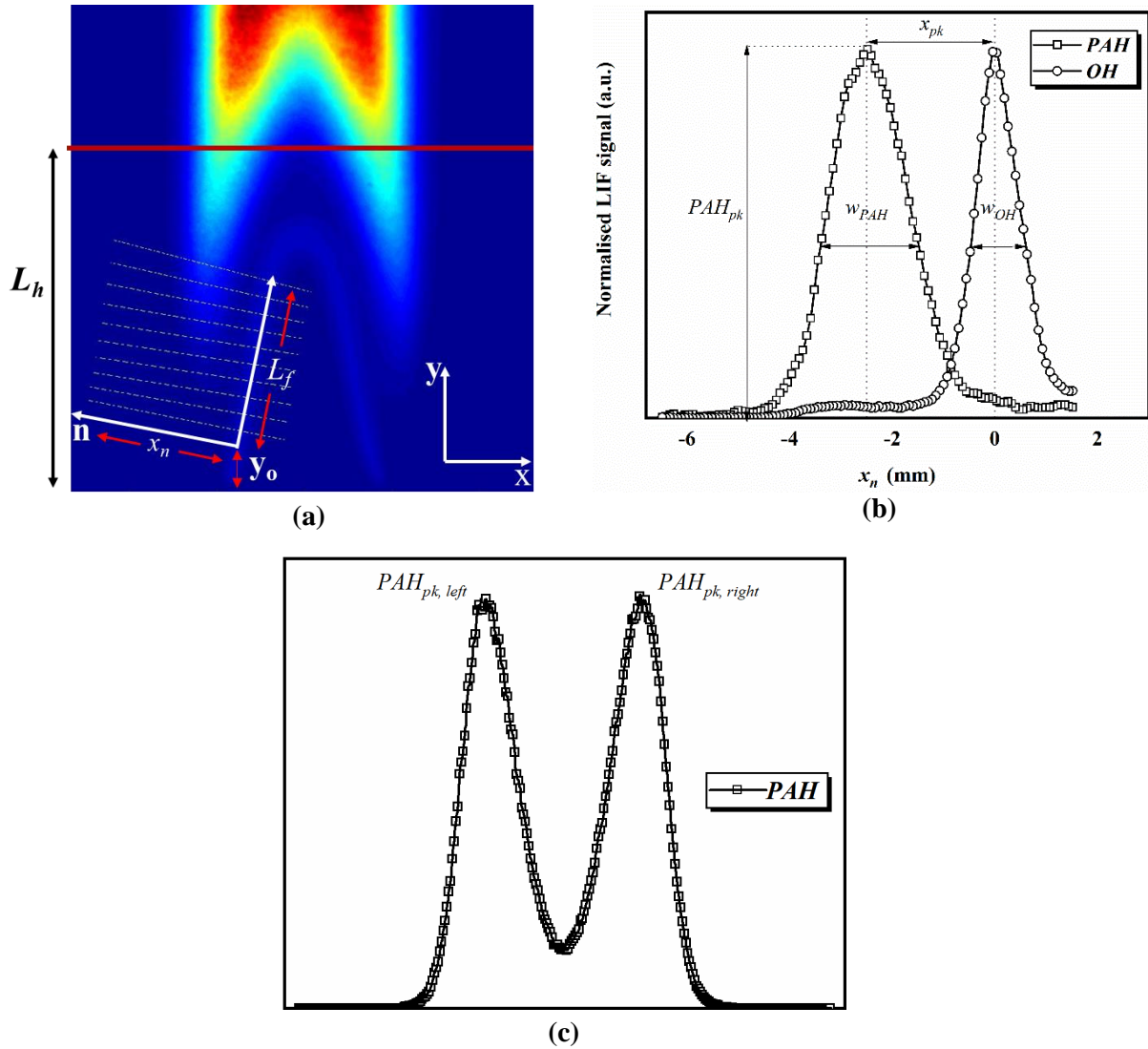

(a)

(b)

(c)

Figure 4: (a) Typical PAH and OH combined LIF image showing the various coordinate systems under consideration, (b) PAH and OH line profile along the normal 'n', at a representative distance of 8 mm along the flame front (L_f) (c) PAH line profile at height 20 mm (at y = L_h in Fig.4a) above the burner lip.

PAH formation is a pyrolytic process, thermal and mass transport effects have a strong influence on PAH concentration profiles. In addition, as the current study utilises hydrogen, which is a relatively fast molecule as compared to methane and air, preferential diffusion effects of molecules can also have significant effects on PAH formation. In non-premixed flames, the peak temperature region coincides with peak OH concentration [49]. Due to the non-availability of well-resolved temperature data, OH will be used as a substitute to denote peak temperature regions. Hence, as one of the image processing approaches, the PAH profiles will be presented based on peak OH location (representing the flame location, that is, peak temperature regions), which would allow meaningful comparison with 1-D simulation.

The reference flame location was evaluated based on the loci of the peak of the OH LIF profile at different heights (referred to as the flame front). A combined (OH and PAH) LIF image is shown in Figure 4a, annotated with the different characteristic parameters used in this work. 'L_f' is the length along of the flame front with respect to a chosen initial height (as shown in Figure 4a), starting at a distance 'y_o' (where y_o = 1.85 mm) above the burner tip. The PAH profile was then determined by walking along a perpendicular axis, n, at every reference location (that is, at various flame front locations 'L_f' along the flame front). 'x_n' indicates distance normal to the flame front (as shown in Figure 4a), and will be used to describe PAH profiles normal to the flame front. The inter-peak distance or peak location (x_{pk}) refers to the distance from the flame front to the maximum PAH LIF signal. The widths of the PAH (w_{PAH}) and OH (w_{OH}) are defined using the full-width half maximums (FWHMs) of their respective profiles. Both parameters, x_{pk} and w_{PAH}, were normalised with w_{OH} along L_f, and have been illustrated in Figure 4b. The change in PAH peak, PAH_{pk}, (or the cumulative, referred as 'PAH_{sum}') of the PAH profile with increasing L_f provided PAH formation characteristics in these flames. The PAH_{sum} refers to the total amount of PAHs (cumulative of PAH profile) along the flame normal, at any given distance along the flame front, L_f. PAH_{sum} incorporates any variation in peak-to-peak distance (x_{pk}), PAH profile width (w_{PAH}) or profile shape at different L_f.

3.2. Change in PAH with vertical height above burner lip

The second image processing approach involved presenting the change in PAH concentration with respect to the vertical height above the burner lip, independent of the flame location. This is because the flame front (represented by the OH profile) only exists up to about 15 mm vertically above the burner tip, and hence to observe PAHs at higher heights it was better to consider the PAH signal independent of the flame front. Figure 4a shows the 'x' and 'y' axis, which refer to the horizontal and vertical Cartesian co-ordinates with respect to the centre of the burner lip. Figure 4c shows a typical line profile at a vertical height of 20 mm above the burner lip; the location of the line profile is shown by the red line (at a height y=L_h) on Figure 4a. A good symmetry can be observed between the LIF signal profile for each side of the flame, providing confidence in the axisymmetric nature of the flame.

From here onwards, the PAH LIF signal and the concentration of PAH (from flame simulation studies) will be referred to as PAH and [PAH] respectively. Similarly, the OH will be denoted by OH and [OH]. PAH_{pk} refers to the maximum LIF signal (profile peak along 'x' and 'n' axes) for each side of the flame, left and right, while PAH_{sum} refers to the cumulative LIF signal for both sides of the flame.

4. Uncertainty and errors

The repeatability of the methodology was verified by performing the same experiments (i.e., using the same test conditions) several times on different days, and the variability in the PAH LIF signals (PAH_{pk} and PAH_{sum}) was determined to be less than 1%. In addition, in order to understand the relationship between laser intensity and PAH LIF signal, a preliminary set of tests were conducted whereby the laser energy was incrementally increased from 3 mJ to 12 mJ, and the PAH LIF signal was found to be independent of laser intensity beyond 8 mJ laser energy. Similar observations regarding saturation of PAH fluorescence to variation in laser fluence have been reported in literature [38]. For this study, the laser energy was kept at 10 mJ, with the laser shot-to-shot energy variations observed to be within ± 10%. This implies that the observed variations in laser energy (that is, 10 ± 1 mJ) are still above the threshold value (8 mJ) for PAH fluorescence saturation. Hence, it can be concluded that the observed differences in PAH LIF signal are independent of fluctuations in laser energy.

To ascertain the effect of the number of images being averaged on the PAH LIF signal and associated noise, up to 800 images were accumulated for the base test condition (methane-only condition), and averages of different number of images were determined. It was concluded that an average of 200 images was sufficient for reliable data analysis, and beyond that point any variation in the signal was negligible. The estimated fluctuations in the distribution of the peak value and the corresponding location was within 3% for the OH and 5% for the PAH, for all test cases. Furthermore, the signal to noise ratio (SNR) evaluated for various conditions ranged from 15 to 18 for OH and 12 to 20 for PAH, with higher SNR for the zoomed in imaging configuration relative to the zoomed out configuration.

5. Results and discussion

### 5.1. Methane-air flame formation characteristics
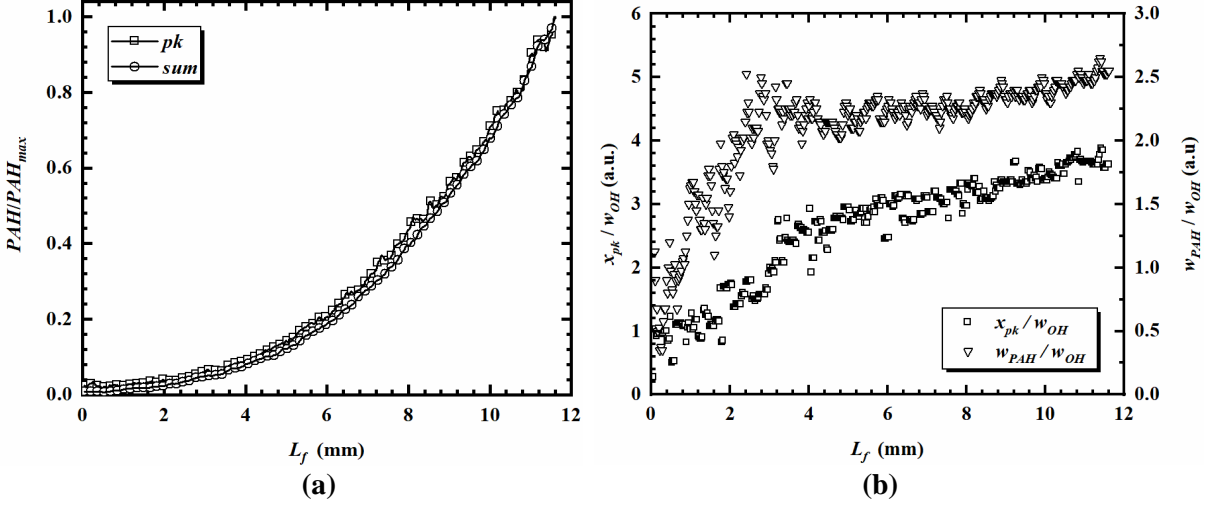
Figure 5: (a) Variation in normalised inter-peak PAH LIF signal (PAH_{pk}) and the cumulative sum of the PAH line profile (PAH_{sum}) as a function of length along the flame front (L_f), and (b) variation in inter-distance between OH peak and PAH peak (x_{pk}), and the PAH profile width (w_{PAH}), normalised with w_{OH}, at various L_f.

Figure 5a shows the change in the peak PAH LIF signal (PAH_{pk}) and the cumulative sum of the PAH line profile (PAH_{sum}) as a function of 'L_f', the distance along the flame front, for the zoomed in imaging configuration. The results shown in Figure 5a are for the methane-air test conditions only, without any addition of H_2. It can be seen that *PAH* increases non-linearly with increasing length along the flame front. The LIF signal from PAH depends on both the number density of each type of PAHs (that is, the PAH concentration), and the structure of the PAH molecule. It is generally known from literature, that larger PAH rings fluoresce with a higher intensity [13,36,50]. Hence, in addition to the increase in the concentration of the PAHs, the increase in LIF signal could also be due to the smaller PAHs combining and growing into larger rings further downstream in the flame. It is pertinent to note that since it was not possible to discriminate between individual PAHs, the signal shown here is only a qualitative indication of PAH formation characteristics in the flame, as described earlier.

Figure 5b presents the variation in the normalised inter-peak distance (x_{pk}) and the normalised PAH profile width (w_{PAH}) with increasing distance along the flame front, L_f; x_{pk} and w_{PAH} were normalised using w_{OH} of the respective profile. The inter-peak distance indicates how far from the flame front does maximum PAH concentration occur with the flame front represented by the loci tracing the peak OH concentration. As explained earlier, the peak *OH* can be approximated to the peak temperature regions with considerable accuracy for non-premixed flames. It can be seen from the figure that inter-peak distance increases almost monotonically with 'L_f'. However, the profile width (w_{PAH}) increases significantly till about 4 mm along the flame front. Up to 4 mm, the signal intensity is weak and the

signal-to-noise ratio (SNR) is relatively low, due to low levels of PAH present and the limitations of the imaging system. Furthermore, the effects of heat loss are more significant close to the lip of the burner. Above 4 mm, the width increases, but not as sharply, indicating the role of continued production of PAHs. As evidenced from 1D flame simulations, PAH production is restricted to a fixed temperature range irrespective of H_2 addition levels (see Table 1), the change in x_{pk} and the w_{PAH} with increasing L_f indicates the effect of residence time. It should also be noted that the similarity in trends of PAH_{sum} and PAH_{pk}, as observed in Figure 5a, exists because the profile width remains largely the same above 4 mm. Hence, only the height of the PAH profile was changing, with increasing length along the flame front, denoting higher LIF signal.
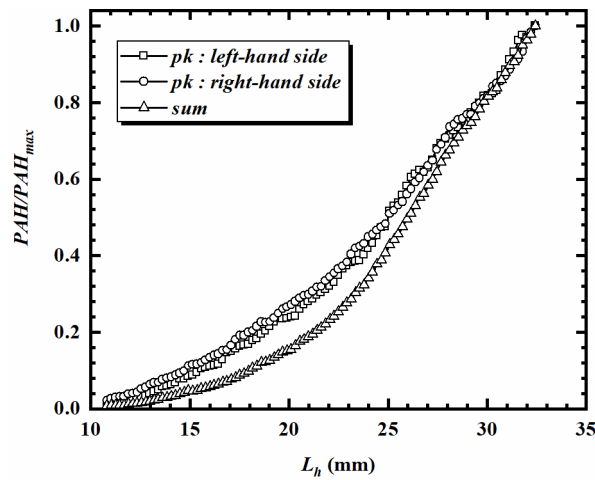
Figure 6: Peak PAH LIF signal (PAH_{pk}) for the left and right sides of the flame, and the cumulative sum of PAH line profile (PAH_{sum}) as a function of the vertical height (L_h) above the burner lip.

Figure 6 shows the change in the peak PAH LIF signal (PAH_{pk}) and the cumulative line profile (PAH_{sum}), as a function of vertical height, L_h, above the burner tip, for the zoomed out camera configuration. Similar to Figure 5a, this figure also shows a monotonic increase in both PAH_{pk} and PAH_{sum} with increasing distance from the burner lip. Similar trends of PAH concentration with respect to height above the burner have been observed in previous studies [49,51,52]. For the zoomed out configuration, since the camera lens was placed further away from the burner (in order to look at PAHs higher up the flame), the amount of light entering the camera lens from the flame was reduced (following the inverse square law relation between intensity and distance from the light source). Hence, no appreciable PAH signal was observed below $L_h = 11$ mm for this configuration. It can also be observed from Figure 6a that both the magnitude and variation in PAH_{pk} evaluated for both sides of the flame (left and right) are similar, which confirms the axisymmetric nature of the burner. Hence, from here onwards, results from only one side of the flame will be presented.

Unlike in Figure 5a, a deviation can be observed between the PAH_{sum} and PAH_{pk} graphs in Figure 6. This is due to the fact that above the conical region (represented by OH), the two sides of the PAH profiles merge to form a bimodal distribution, resulting in variation in trends of PAH_{sum} and $PAH_{pk.}$
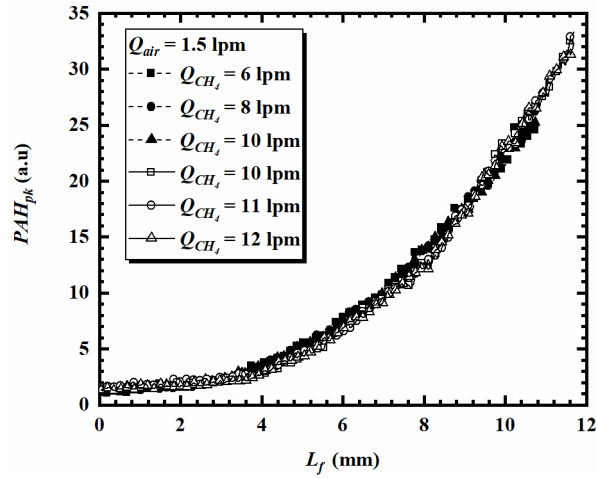
5.2. Effect of methane and air flow rate

Figure 7: Effect of varying the methane (CH₄) flow rate on the PAH LIF signal, for a fixed air flow rate.

Figure 7 shows the effect of variation in methane flow rate, Q_{CH4}, on the peak PAH intensity signal. It can be seen from Figure 7 that when the flow rate of methane is increased from 6 lpm to 12 lpm (a change of 100%), no significant change in *PAH* is obeserved. This shows that the effect of change in convection velocity had negligble influence on the PAH formation characteristics. This could potentially be explained by the fact that the mixing of reactants in IDF configuration is primarily diffusion-controlled. Hence, other factors, such as change in bulk velocity or change in the fluid shear stress (between the central and outer flows) might not have a significant impact. Therefore, when hydrogen is added to the fuel flow (up to 20% of the volume flow rate of methane, Q_{CH4}), it can be safely assumed that the change in PAH characteritics is primarily due to H_2 addition and not a consequence of the variations in bulk velocity values. The rate of change in *PAH* (both peak and sum) with respect to the distance, presented here, is an indicative characteristic of the sooting tendency of the fuel mixture. It is clear from these results, if the air flow rate was kept constant, this *PAH* growth rate (change in PAH LIF signal with respect to L_f or L_h) will allow direct comparison of sooting tendencies (that is, PAH formation potential) of various fuel mixtures.

5.3.   Hydrogen addition to the fuel (CH₄) stream
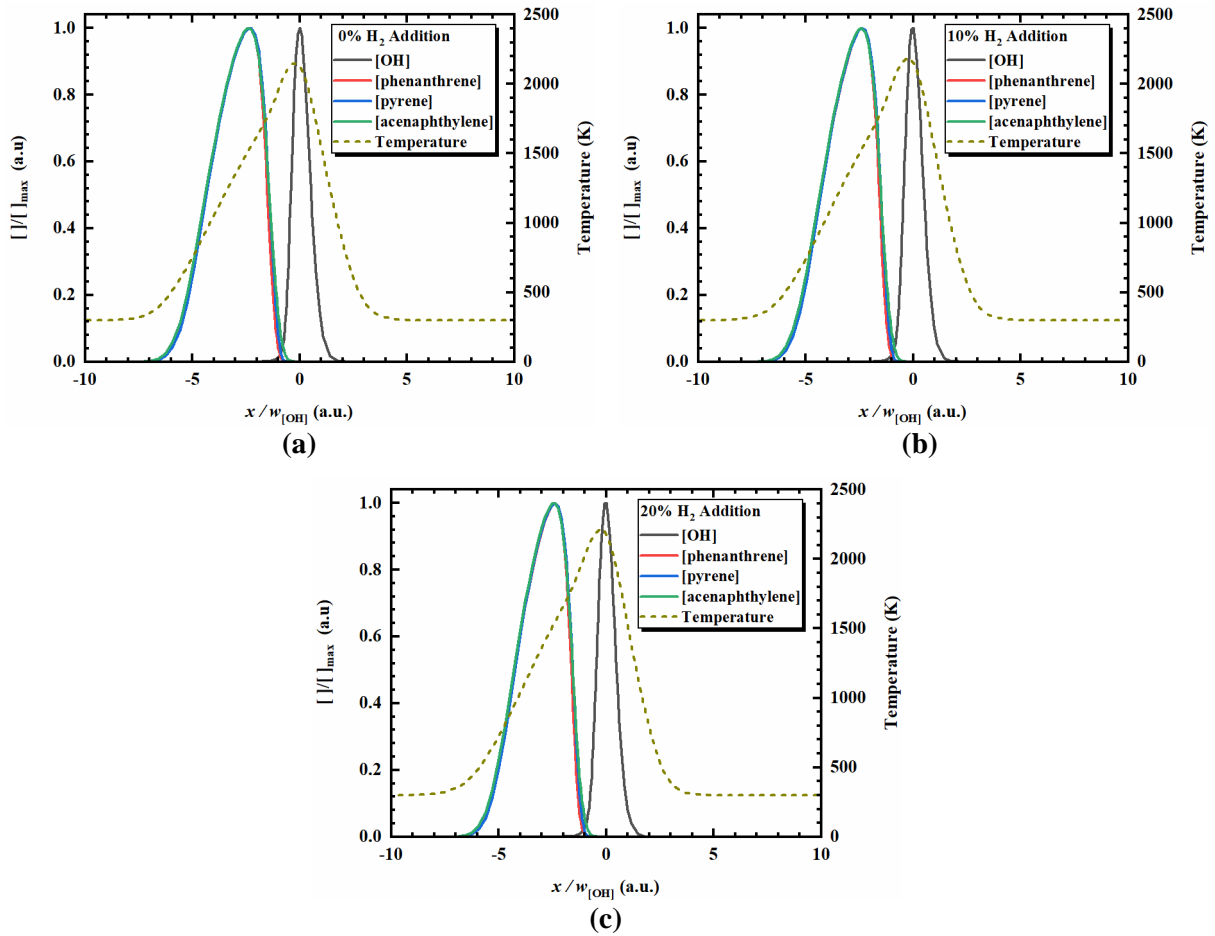
Figure 8: Axial profiles of [OH], three PAH species (3-ring: [phenanthrene], [acenaphthylene] and 4-ring: [pyrene]), and temperature for (a) 0%, (b) 10% and (c) 20% H₂ addition, simulated using 1-D modelling of CH₄-H₂ flame. (Note: '*x*' distance is normalised with FWHM of OH concentration, $w_{[OH]}$)

Figure 8 shows the axial profile concentrations of OH, temperature and three PAH species – phenanthrene (3 rings), acenaphthylene (3 rings) and pyrene (4 rings) – for three different H₂ additions (0, 10 and 20%), obtained from 1-D simulations of the methane-hydrogen flame. Simulation results for other mixture conditions are available, but for brevity only three conditions are presented. To allow accurate comparison, the x-axis has been normalised with respect to the full width-half maximum (FWHM) value of the OH profile, $w_{[OH]}$. No significant change in the PAH line profile shape is observed with increasing levels of H₂ addition. As expected, the peak temperature does show an increase, but only of about 50-70 K with increasing levels of H₂ (maximum temperature data also shown in Table 1).
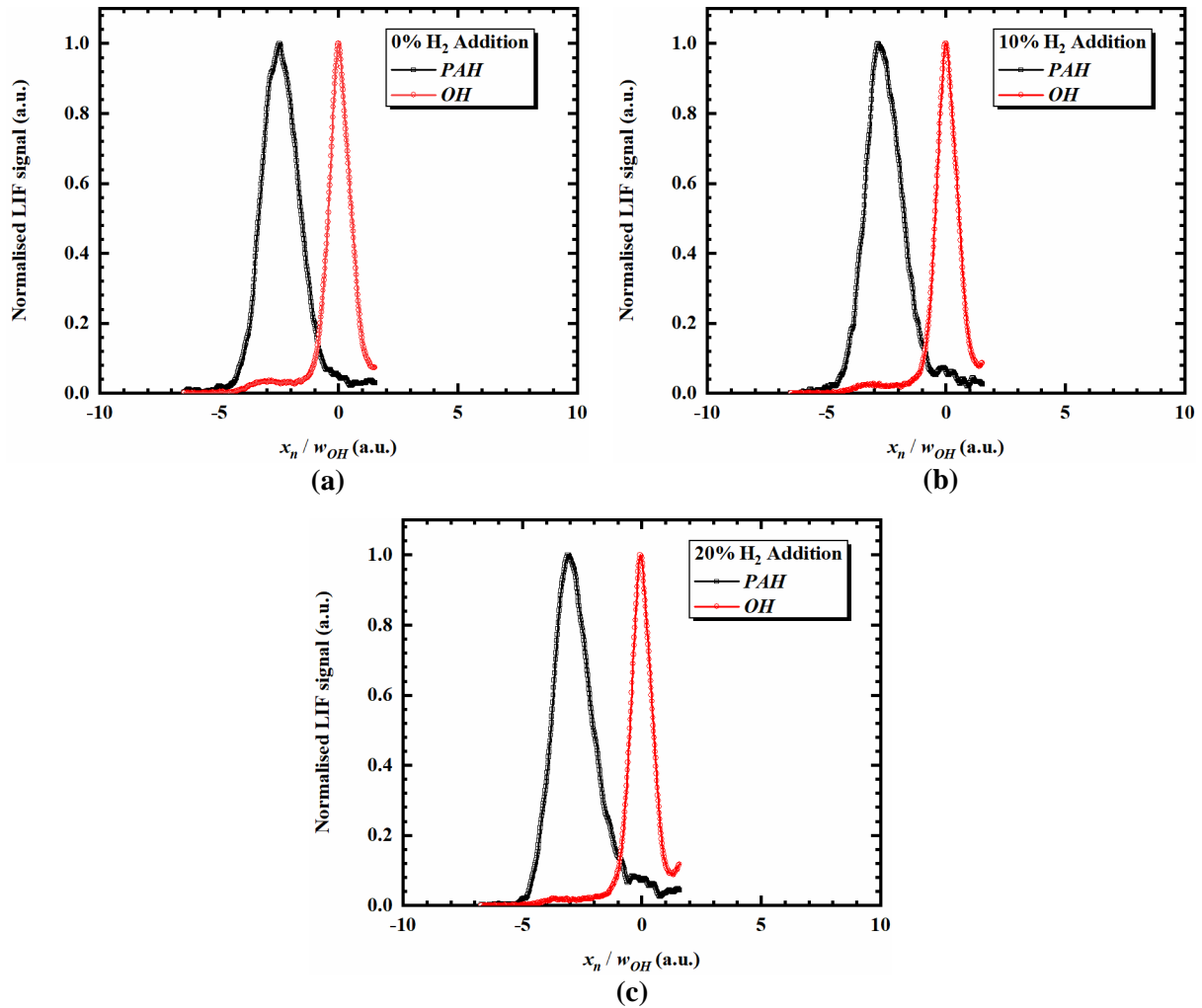
Figure 9: Line profiles of LIF signals *OH* and *PAH* along the normal, at a distance of 8 mm along the flame front (L_f) for (a) 0%, (b) 10% and (c) 20% H₂ addition.

Figure 9 shows the line profiles of *OH* and *PAH* species for three different H$_2$ additions (0, 10 and 20%) from experiments, obtained perpendicular to the flame front, at a length of 8 mm along the flame front. Similar to Figure 8, the x-axis for Figure 9 has also been normalised with respect to the FWHM value of the OH line profile, w_{OH}. A number of similarities can be observed between the computational and experimental line profiles presented in Figure 8 and 9. The normalised experimental PAH profiles similar to PAH concentration profiles from simulation start to increase at about 1 (a.u.) on the fuel side, away from the peak OH location for both sets of data. The experiments are limited in terms of resolving between individual PAH species, however the computational data shows that the different 3 and 4 ring PAH species have almost identical line profiles and are similarly affected by H$_2$. Hence, the experimental data can be used to represent PAHs of a certain size group with reasonable accuracy.
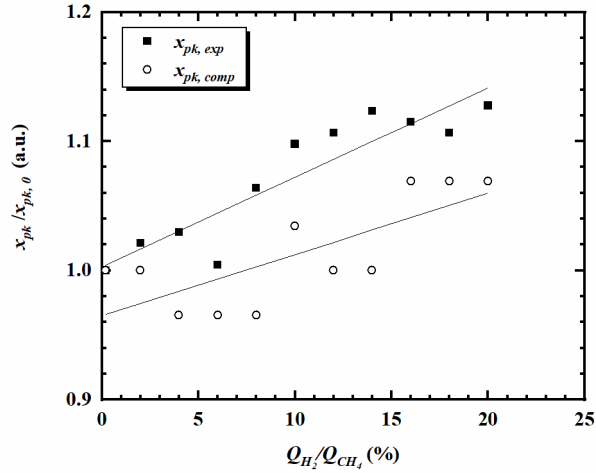
Figure 10: Comparison of the distance between OH peak and PAH peak (x_{pk}) normalised with base case value ($x_{pk,\,0}$), for various H$_2$ addition levels in the methane flame, for both experimental and 1-D flame simulation studies. For experiments, data was obtained at a distance of 8 mm along the flame front ($L_f = 8mm$).
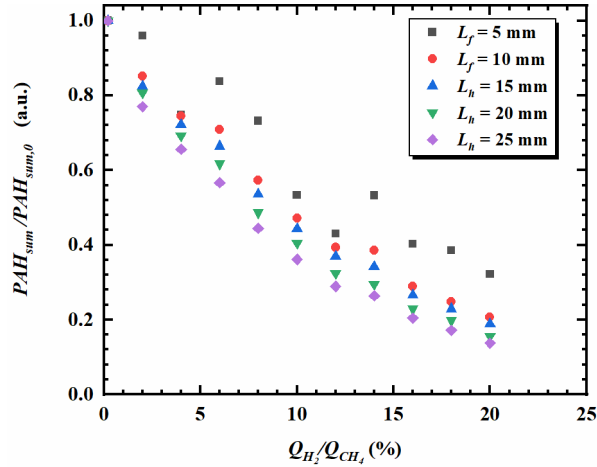
Figure 10 shows the variation in the normalised distance between the OH and the PAH peaks against different levels of H$_2$ addition in the fuel (CH$_4$) stream, for experimental ($x_{pk,exp}$) and 1-D flame simulation ($x_{pk,comp}$) studies, at a distance of 8 mm along the flame front, L_f. The inter-peak distance x_{pk} was normalised with the x_{pk} values of the base case, $x_{pk,\,0}$ (that is, 100% CH$_4$ and 0% H$_2$). It can be seen from the figure that both $x_{pk,exp}$ and $x_{pk,comp}$ show an overall increase with H$_2$ addition. This observed trend is due to variations in adiabatic flame temperatures. Additionally, in an IDF configuration (present experimental work) combustion products and the unburnt fuel interact, which could potentially result in increased local mixture temperatures. The differences observed in the experimental and computational results could be attributed to the differences in flame configurations (2-D for experimental and 1-D for computational).
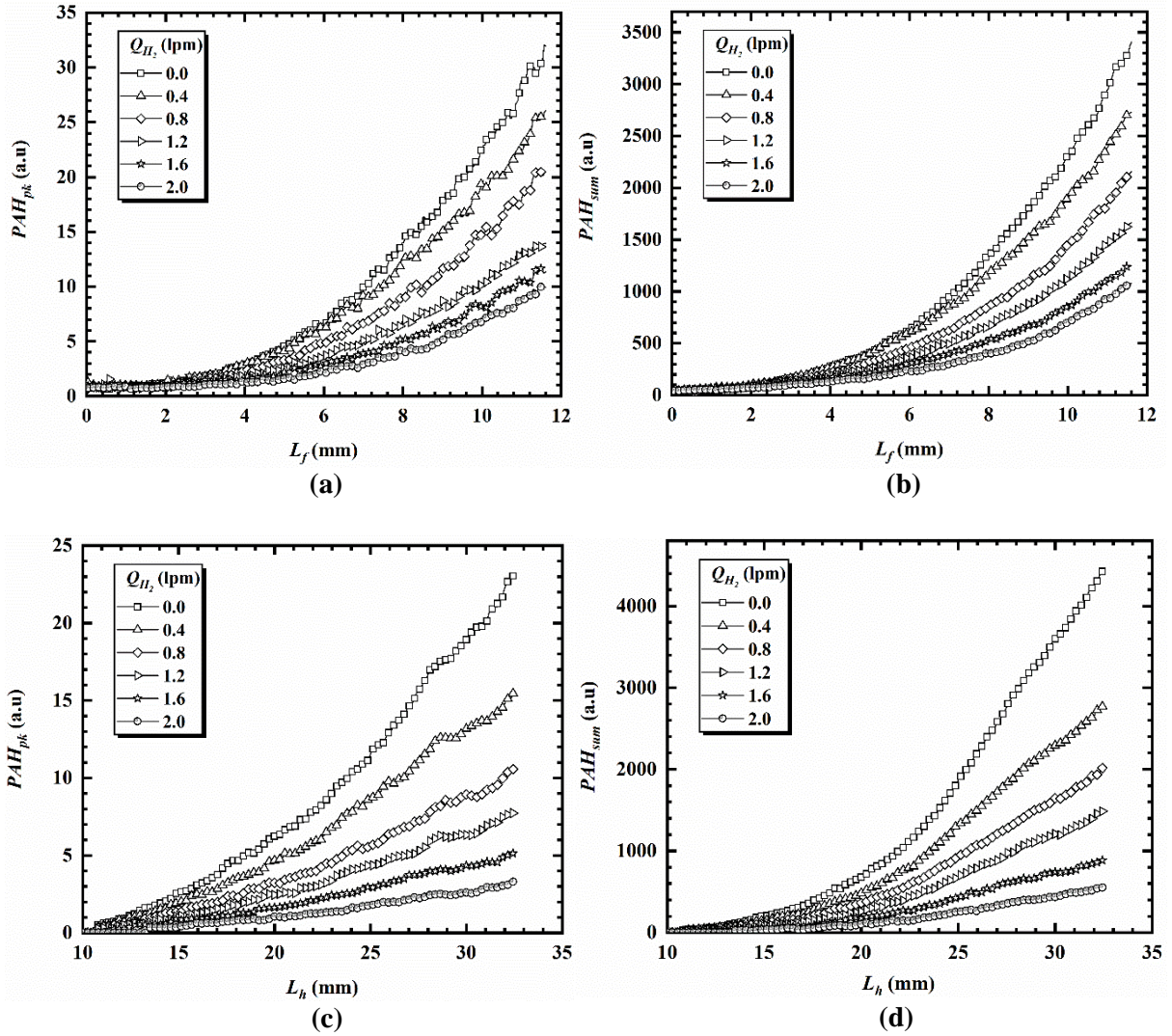
Figure 11: (a) Peak PAH LIF signal (*PAH$_{pk}$*) and (b) cumulative sum of PAH line profile (*PAH$_{sum}$*) as a function of *L$_f$* (length along the flame front), and (c) *PAH$_{pk}$* and (d) *PAH$_{sum}$* as a function of *L$_h$* (vertical height above the burner lip), for various H$_2$ addition levels.

Figure 11 shows the *PAH$_{pk}$* and *PAH$_{sum}$* for both the zoomed in (11a and 11b) and zoomed out (11c and 11d) camera configurations, for different levels of H$_2$ addition in the fuel (CH$_4$) stream. The zoomed in data is presented as a function of distance along the flame front (*L$_f$*), while the zoomed out data has been presented as a function of vertical height above the burner (*L$_h$*), and shows PAHs at higher heights as compared to the zoomed in graphs. It can be observed from Figure 11a that the change in the PAH signal w.r.t. the length of the flame front is highest for the methane only flame, that is, without any H$_2$ addition. As H$_2$ is incrementally added, the rate of increase of *PAH$_{pk}$* with respect to *L$_f$*, reduces. Similar trend in the reduction of *PAH* with H$_2$ is also observed at higher heights above the burner tip (Figure 11c-zoomed out configuration), as well as in the *PAH$_{sum}$* graphs for both the configurations (Figures

11b and 11d). This characteristic reduction in *PAH* with H$_2$ addition will be further discussed in the next few paragraphs.

Figure 12: Variation in the *PAH$_{sum}$* LIF signal normalised using base case value (*PAH$_{sum,0}$*), as a function of percentage H$_2$ addition, at five different heights above the burner lip.

Figure 12 shows the variation in the *PAH$_{sum}$* at five fixed heights above the burner lip (*L$_f$* in the case of the 'zoomed in' configuration and *L$_h$* in the case of the 'zoomed out' configuration), as a function of H$_2$ addition. The *PAH$_{sum}$* values have been normalised against the base case, *PAH$_{sum,0}$* (that is, 100% CH$_4$ and 0% H$_2$). It can be seen from the Figure 12 that *PAH$_{sum}$* reduces monotonically with H$_2$ addition at all the heights presented. Considering the reduction in the PAH signal due to H$_2$ addition, it can be observed that at the lowest height presented of 5 mm (*L$_f$*) the change in the *PAH$_{sum}$* is relatively lower (70%) as compared to at the highest height where a reduction of almost 90% was observed with at the highest H$_2$ addition level. As noted in previous studies, larger PAHs form at higher heights above the burner [49,51,52]. Since the addition of H$_2$ impedes the formation of smaller PAHs, and hence preventing the formation of the larger PAHs, the effect of H$_2$ addition is more significant at higher heights.
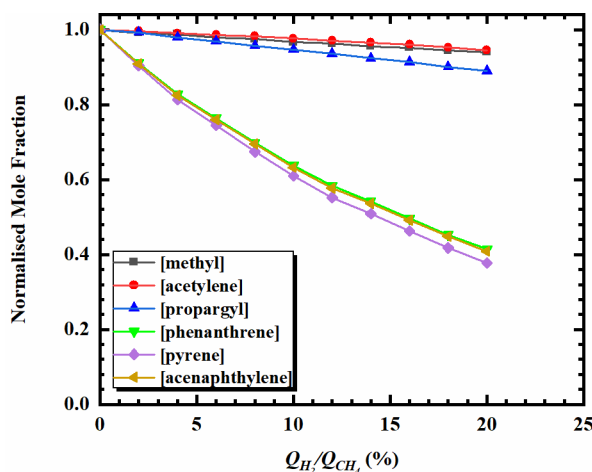
Figure 13: Variation in the concentrations of six species - methyl, acetylene, propargyl, acenaphthylene, phenanthrene, pyrene – as a function of H_2 addition in fuel (CH_4) stream, simulated using 1-D modelling.

Figure 13 shows the variation in the concentrations of six species - methyl, acetylene, propargyl, acenaphthylene, phenanthrene, pyrene – as a function of H_2 addition in fuel (CH_4) stream, simulated using 1-D computational modelling. It can be seen from the figure that the addition of H_2 results in an almost 5% reduction in methyl and acetylene, about 10% reduction in propargyl and a corresponding 60% reduction in the three PAH species. Acetylene and propargyl are important species for the formation of first ring, benzene (C_6H_6), which itself is an important intermediate for subsequent formation of larger rings [53,54]. Both acetylene and propargyl are building blocks of PAHs, involved in the primary reaction pathways of PAH formation. Acetylene is a crucial species of the HACA (hydrogen abstraction-acetylene addition) mechanism of PAH growth, while the recombination of propargyl is considered to be the most important cyclisation reaction in hydrocarbon flames [52,55–57]. Hence, a reduction in the concentration of acetylene and propargyl can have a significant impact on the concentration of the larger species like acenaphthylene, phenanthrene and pyrene, as can be observed in Figure 13.

The reduction in PAHs with H_2 addition, as observed in both Figures 12 and 13, could be attributed to the added H_2 chemically inhibiting PAH formation. The mole fraction of OH has been observed to increase with H_2 addition to the fuel stream, both in this work and in previous studies [26,58]. Hence, it can be assumed that the increase in OH radicals could result in an increase in the rate of reactions which lead to higher oxidation rates of both acetylene and propargyl, hence reducing their availability to take part in the PAH formation reactions, and suppressing subsequent growth of PAHs. Another chemical effect associated with increasing the amount of H_2 in the reacting zone is the increase in the reverse rate of the H-abstraction reaction ($R_1 + H \leftrightarrow R_2 + H_2$), which is a key reaction whereby H-abstraction takes place to allow acetylene addition [59,60]. The abstraction of H atoms activates the surface sites of PAHs, and various hydrocarbon species such as acetylene and other PAHs then react with these active sites, hence propagating the surface growth process. The reduced H-abstraction reaction rate reduces the number of sites available for acetylene addition, inhibiting surface growth of

PAHs. Comparing Figures 12 and 13, it can be observed that the reduction in PAH_{sum} at 5 mm along L_f with maximum H_2 addition is about 70%, which is quite similar to the reduction in PAH concentration (approximately 60%) observed from the flame simulation studies for the same H_2 addition.

Conclusions

This paper presented an experimental methodology to analyse PAH formation characteristics in non-premixed methane-air flames with systematic H_2 addition, in an inverse diffusion flame, IDF, configuration. Simultaneous OH and PAH PLIF measurements were performed, and the PAH characteristics were described in relation to the OH profiles (which represented maximum temperature locations). This methodology enabled a comprehensive study of PAH formation characteristics with incremental H_2 addition in non-premixed flames, and allowed meaningful comparisons to be made between the experiments and 1-D flame simulations. Some specific conclusions on the effect of H_2 addition on PAH formation from this work are:

1. *PAH* increased with increasing height above the burner attributed to both higher concentration of PAHs as well as formation of larger rings.
2. The distance between the OH and PAH peaks was observed to increase with increasing height above the burner. However, the PAH profile width remained largely similar beyond 4 mm above the burner tip. The change in the width below 4 mm was attributed to the radiative effects due to close proximity to the burner lip.
3. When considering H_2 addition, both experimental and computational results showed similar PAH profile widths, with no significant change observed with H_2 addition. However, the peak PAH location from the experimental campaign was observed to shift slightly away from the OH peak (representing maximum temperature locations) with increasing H_2 addition.
4. The rate of change in *PAH* with respect to the length of flame front (or height above burner) was highest for the methane only condition, with this rate reducing as H_2 was incrementally added.
5. The reduction in *PAH* was observed to be monotonic with H_2 addition at all the heights above the burner tip, with higher reductions observed at higher heights above the burner. This was attributed to H_2 preventing the formation of smaller PAHs at lower heights which would in turn impede the formation of larger PAHs at higher heights.
6. The percentage reduction in *PAH* with H_2 addition at 5 mm above the burner tip was of similar magnitude to that observed from 1-D flame simulations. This is because the 1-D flame simulations cannot capture resident time, and hence are most comparable to heights closer to the burner tip but away from high strain and heat loss region.
7. The reduction in *PAH* with H_2 addition was attributed to the increased oxidation of crucial species, such as acetylene and propargyl, hence reducing their availability for key PAH formation pathways. In addition, H_2 reduced the rate of H-abstraction, hence impeding growth reactions on PAHs due to reduction of active sites for PAH growth.

Acknowledgements

Nomenclature

CH_4	Methane
FOV	Field of view
FWHM	Full Width Half Maximum
HACA	Hydrogen Abstraction-Acetylene Addition
H_2	Hydrogen
ICCDs	Intensified Charge Coupled Devices
IDF	Inverse Diffusion Flames
L_f	Distance along the flame front
L_h	Height above the burner
lpm	Litres per minute
NDF	Normal Diffusion Flames
OH	Hydroxyl radical
PAH	Polycyclic Aromatic Hydrocarbons
PAH_{pk}	Peak value of PAH LIF profile
PAH_{sum}	Cumulative of PAH LIF profile
PLIF	Planar Laser Induced Fluorescence
Q	Volume flow rate
ROI	Region of Interest
SNR	Signal to Noise Ratio
w_{PAH}	FWHM of the experimental PAH profile
w_{OH}	FWHM of the experimental OH profile
$w_{[OH]}$	FWHM of computational OH profile
x_{pk}	The inter-peak distance between OH and PAH
$x_{pk,0}$	The inter-peak distance x_{pk} for pure methane case

References

[1]   Lunde G, Bjorseth A. Polycyclic aromatic hydrocarbons in long-range transported aerosols. Nature 1977;268:518–9. doi:10.1038/268518a0.

[2]   Abdel-Shafy HI, Mansour MSM. A review on polycyclic aromatic hydrocarbons: Source, environmental impact, effect on human health and remediation. Egypt J Pet 2016;25:107–23. doi:10.1016/j.ejpe.2015.03.011.

[3]   Harvey R. Polycyclic Aromatic Hydrocarbons: Chemistry and Carcinogenicity. 1st ed. Cambridge: Cambridge University Press; 1991.

[4]   Velásquez M, Mondragón F, Santamaría A. Chemical characterization of soot precursors and soot particles produced in hexane and diesel surrogates using an inverse diffusion flame burner. Fuel 2013;104:681–90. doi:10.1016/j.fuel.2012.04.033.

[5]   Santamaría A, Mondragón F, Molina A, Marsh ND, Eddings EG, Sarofim AF. FT-IR and1H NMR characterization of the products of an ethylene inverse diffusion flame. Combust Flame 2006;146:52–62. doi:10.1016/j.combustflame.2006.04.008.

[6]   Shaddix CR, Williams TC. Measurements of the velocity field in laminar ethylene inverse jet diffusion flames. Combust Flame 2009;156:942–5. doi:10.1016/j.combustflame.2009.01.017.

[7]   Mikofski MA, Williams TC, Shaddix CR, Blevins LG. Flame height measurement of laminar inverse diffusion flames. Combust Flame 2006;146:63–72. doi:10.1016/j.combustflame.2006.04.006.

[8]   Yamamoto K, Takemoto M. Reductions of PAH and Soot by Center Air Injection. Environments 2014;1:42–53. doi:10.3390/environments1010042.

[9]   Liu F, Hua Y, Wu H, Lee CFF, Li Y. Experimental investigation of polycyclic aromatic hydrocarbons growth characteristics of gasoline mixed with methanol, ethanol, or n-butanol in laminar diffusion flames. Energy and Fuels 2018;32:6823–33. doi:10.1021/acs.energyfuels.8b00693.

[10]   Zhang Y, Wang L, Liu P, Guan B, Ni H, Huang Z, et al. Experimental and kinetic study of the effects of CO2and H2O addition on PAH formation in laminar premixed C2H4/O2/Ar flames. Combust Flame 2018;192:439–51. doi:10.1016/j.combustflame.2018.01.050.

[11]   Wu J, Song KH, Litzinger T, Lee SY, Santoro R, Linevsky M. Reduction of PAH and soot in premixed ethylene-air flames by addition of dimethyl ether. Combust Sci Technol 2006;178:837–63. doi:10.1080/00102200500269942.

[12]   Sidebotham GW, Glassman I. Flame temperature, fuel structure, and fuel concentration effects on soot formation in inverse diffusion flames. Combust Flame 1992;90:269–83. doi:10.1016/0010-2180(92)90088-7.

[13]   Bejaoui S, Mercier X, Desgroux P, Therssen E. Laser induced fluorescence spectroscopy of aromatic species produced in atmospheric sooting flames using UV and visible excitation wavelengths. Combust Flame 2014;161:2479–91. doi:10.1016/j.combustflame.2014.03.014.

[14]   Blevins LG, Fletcher RA, Benner BA, Steel EB, Mulholland GW. The existence of young soot in the exhaust of inverse diffusion flames. Proc Combust Inst 2002;29:2325–33. doi:10.1016/S1540-7489(02)80283-8.

[15]   Dobbins RA. Hydrocarbon nanoparticles formed in flames and diesel engines. Aerosol Sci Technol 2007;41:485–96. doi:10.1080/02786820701225820.

[16]   Hansen N, Cool TA, Westmoreland PR, Kohse-Höinghaus K. Recent contributions of flame-sampling molecular-beam mass spectrometry to a fundamental understanding of combustion chemistry. Prog Energy Combust Sci 2009;35:168–91. doi:10.1016/j.pecs.2008.10.001.

[17]   Ju EL, Oh KC, Shin HD. Soot formation in inverse diffusion flames of diluted ethene. Fuel 2005;84:543–50. doi:10.1016/j.fuel.2004.11.003.

[18]   Yamamoto K, Takemoto M. Measurement of PAH and soot of diffusion flames in a triple port burner. Fuel Process Technol 2013;107:99–106. doi:10.1016/J.FUPROC.2012.06.006.

[19]   Choi SK, Choi BC, Lee SM, Choi JH. The effect of liquid fuel doping on PAH and soot formation in counterflow ethylene diffusion flames. Exp Therm Fluid Sci 2015;60:123–31. doi:10.1016/j.expthermflusci.2014.08.008.

[20]   Golea D, Rezgui Y, Guemini M, Hamdane S. Reduction of PAH and soot precursors in benzene flames by addition of ethanol. J Phys Chem A 2012;116:3625–42. doi:10.1021/jp211350f.

[21]   Singh P, Sung CJ. PAH formation in counterflow non-premixed flames of butane and butanol isomers. Combust Flame 2016;170:91–110. doi:10.1016/j.combustflame.2016.05.009.

[22]   Choi J-H, Hwang C-H, Choi SK, Lee SM, Lee WJ, Jang SH, et al. Impacts of hydrogen addition on micro and nanostructure of soot particles formed in C2H4/air counter diffusion flames. Int J Hydrogen Energy 2016;41:15852–8. doi:10.1016/J.IJHYDENE.2016.04.158.

[23]   Mze Ahmed A, Mancarella S, Desgroux P, Gasnot L, Pauwels J-F, El Bakali A. Experimental and numerical study on rich methane/hydrogen/air laminar premixed flames at atmospheric pressure: Effect of hydrogen addition to fuel on soot gaseous precursors. Int J Hydrogen Energy 2016;41:6929–42. doi:10.1016/J.IJHYDENE.2015.11.148.

[24]   De Iuliis S, Maffi S, Migliorini F, Cignoli F, Zizak G. Effect of hydrogen addition on soot formation in an ethylene/air premixed flame. Appl Phys B Lasers Opt 2012;106:707–15. doi:10.1007/s00340-012-4903-2.

[25]   Gu M, Chu H, Liu F. Effects of simultaneous hydrogen enrichment and carbon dioxide dilution of fuel on soot formation in an axisymmetric coflow laminar ethylene/air diffusion flame. Combust Flame 2016;166:216–28. doi:10.1016/j.combustflame.2016.01.023.

[26]   Guo H, Liu F, Smallwood GJ, Gülder ÖL. Numerical study on the influence of hydrogen addition on soot formation in a laminar ethylene-air diffusion flame. Combust Flame 2006;145:324–38. doi:10.1016/j.combustflame.2005.10.016.

[27]   Gülder ÖL, Snelling DR, Sawchuk RA. Influence of hydrogen addition to fuel on temperature field and soot formation in diffusion flames. Symp Combust 1996;26:2351–8. doi:10.1016/S0082-0784(96)80064-6.

[28]   Park S, Wang Y, Chung SH, Sarathy SM. Compositional effects on PAH and soot formation in counterflow diffusion flames of gasoline surrogate fuels. Combust Flame 2017;178:46–60. doi:10.1016/j.combustflame.2017.01.001.

[29]   Lee SM, Yoon SS, Chung SH. Synergistic effect on soot formation in counterflow diffusion flames of ethylene-propane mixtures with benzene addition. Combust Flame 2004;136:493–500. doi:10.1016/j.combustflame.2003.12.005.

[30] Wei M, Liu J, Guo G, Li S. The effects of hydrogen addition on soot particle size distribution functions in laminar premixed flame. Int J Hydrogen Energy 2016;41:6162–9. doi:10.1016/J.IJHYDENE.2015.10.022.

[31] Liu F, Ai Y, Kong W. Effect of hydrogen and helium addition to fuel on soot formation in an axisymmetric coflow laminar methane/air diffusion flame. Int J Hydrogen Energy 2014;39:3936–46. doi:10.1016/j.ijhydene.2013.12.151.

[32] Yuan C, Han C, Liu Y, He Y, Shao Y, Jian X. Effect of hydrogen addition on the combustion and emission of a diesel free-piston engine. Int J Hydrogen Energy 2018;43:13583–93. doi:10.1016/j.ijhydene.2018.05.038.

[33] Koten H. Hydrogen effects on the diesel engine performance and emissions. Int J Hydrogen Energy 2018;43:10511–9. doi:10.1016/j.ijhydene.2018.04.146.

[34] Talibi M, Balachandran R, Ladommatos N. Influence of combusting methane-hydrogen mixtures on compression–ignition engine exhaust emissions and in-cylinder gas composition. Int J Hydrogen Energy 2017;42:2381–96. doi:10.1016/j.ijhydene.2016.10.049.

[35] Park SH, Lee KM, Hwang CH. Effects of hydrogen addition on soot formation and oxidation in laminar premixed C2H2/air flames. Int J Hydrogen Energy 2011;36:9304–11. doi:10.1016/j.ijhydene.2011.05.031.

[36] Zizak G, Cignoli F, Montas G, Beneccchi S, Dondè R. Detection of aromatyc hydrocabons in the exhaust gases of a i.c. engine by laser-induced fluorescence technique. Recent Res Devel Appl Spectro 1996;1.

[37] Xiao J, Austin E, Roberts WL. Relative polycyclic aromatic hydrocarbon concentrations in unsteady counterflow diffusion flames. Combust Sci Technol 2005;177:691–713. doi:10.1080/00102200590917239.

[38] Vander Wal RL. LIF-LII measurements in a turbulent gas-jet flame. Exp Fluids 1997;23:281–7. doi:10.1007/s003480050112.

[39] Chakraborty A, Chakravarthy SR. Formation of Soot in Ethylene – Air Partially Premixed Flames Over a Wide Range of Premixedness. J Eng Gas Turbines Power 2018;139:1–6. doi:10.1115/1.4037580.

[40] Berman IR. Handbook of Fluorescence Spectra of Aromatic Molecules. second edi. New York: Academic Press; 1971.

[41] Wang Y, Park S, Sarathy SM, Chung SH. A comparative study on the sooting tendencies of various 1-alkene fuels in counterflow diffusion flames. Combust Flame 2018;192:71–85. doi:10.1016/j.combustflame.2018.01.033.

[42] Ciajolo A, Tregrossi A, Barbella R, Ragucci R, Apicella B, de Joannon M. The relation between ultraviolet-excited fluorescence spectroscopy and aromatic species formed in rich laminar ethylene flames. Combust Flame 2001;125:1225–9. doi:10.1016/S0010-2180(01)00242-5.

[43] Verhoeven LM, de Andrade Oliveira MH, Lantz A, Li B, Li ZS, Luijten CCM, et al. A numerical and experimental study of Polycyclic Aromatic Hydrocarbons in a laminar diffusion flame. Proc Combust Inst 2013;34:1819–26. doi:10.1016/J.PROCI.2012.06.016.

[44] Vander Wal RL, Jensen KA, Choi MY. Simultaneous laser-induced emission of soot and polycyclic aromatic hydrocarbons within a gas-jet diffusion flame. Combust Flame

1997;109:399–414. doi:10.1016/S0010-2180(96)00189-7.

[45]   Eckbreth AC. Laser Diagnostics for Combustion Temperature and Species. 2nd ed. Amsterdam: Gordon and Breach Publishers; 1996.

[46]   Smyth KC, Shaddix CR, Everest DA. Aspects of soot dynamics as revealed by measurements of broadband fluorescence and flame luminosity in flickering diffusion flames. Combust Flame 1997;111:185–207. doi:10.1016/S0010-2180(97)00017-5.

[47]   Goodwin DG, Moffat HK, Speth RL. Cantera: An Object-oriented Software Toolkit for Chemical Kinetics, Thermodynamics, and Transport Processes. Version 2.2.0 2017. doi:10.5281/zenodo.48735.

[48]   Appel J, Bockhorn H, Frenklach M. Kinetic modeling of soot formation with detailed chemistry and physics: laminar premixed flames of C2 hydrocarbons. Combust Flame 2000;121:122–36. doi:10.1016/S0010-2180(99)00135-2.

[49]   Mikofski MA, Williams TC, Shaddix CR, Fernandez-Pello AC, Blevins LG. Structure of laminar sooting inverse diffusion flames. Combust Flame 2007;149:463–78. doi:10.1016/J.COMBUSTFLAME.2007.01.006.

[50]   Beretta F, Cincotti V, D'Alessio A, Menna P. Ultraviolet and visible fluorescence in the fuel pyrolysis regions of gaseous diffusion flames. Combust Flame 1985;61:211–8. doi:10.1016/0010-2180(85)90102-6.

[51]   Hepp H, Siegmann K, Sattler K. New aspects of growth mechanisms for polycyclic aromatic hydrocarbons in diffusion flames. Chem Phys Lett 1995;233:16–22. doi:10.1016/0009-2614(94)01433-V.

[52]   Richter H, Howard J. Formation of polycyclic aromatic hydrocarbons and their growth to soot - a review of chemical reaction pathways. Prog Energy Combust Sci 2000;26:565–608. doi:10.1016/S0360-1285(00)00009-5.

[53]   Bockhorn H, Schäfer T. Growth of Soot Particles in Premixed Flames by Surface Reactions, 1994, p. 253–74. doi:10.1007/978-3-642-85167-4_14.

[54]   Wang H, Frenklach M. A detailed kinetic modeling study of aromatics formation in laminar premixed acetylene and ethylene flames. Combust Flame 1997;110:173–221. doi:10.1016/S0010-2180(97)00068-0.

[55]   Frenklach M, Wang H. Detailed modeling of soot particle nucleation and growth. Symp Combust 1991;23:1559–66. doi:10.1016/S0082-0784(06)80426-1.

[56]   Kislov V V., Sadovnikov AI, Mebel AM. Formation Mechanism of Polycyclic Aromatic Hydrocarbons beyond the Second Aromatic Ring. J Phys Chem A 2013;117:4794–816. doi:10.1021/jp402481y.

[57]   Miller JA, Melius CF. Kinetic and thermodynamic issues in the formation of aromatic compounds in flames of aliphatic fuels. Combust Flame 1992;91:21–39. doi:10.1016/0010-2180(92)90124-8.

[58]   PANDEY P, PUNDIR B, PANIGRAHI P. Hydrogen addition to acetylene–air laminar diffusion flames: Studies on soot formation under different flow arrangements. Combust Flame 2007;148:249–62. doi:10.1016/j.combustflame.2006.09.004.

[59]   Park S-H, Choi MY, Yozgatligil A. Nanostructure of Soot Collected from Ethanol Droplet Flames in Microgravity. Combust Sci Technol 2009;181:1164–86. doi:10.1080/00102200903074154.

[60]   Frenklach M. Reaction mechanism of soot formation in flames. Phys Chem Chem Phys 2002;4:2028–37. doi:10.1039/b110045a.